A Colorimetric Label-Free Sensor Array of Metal–Organic-Framework-Based Fabry–Pérot Films for Detecting Volatile Organic Compounds and Food Spoilage

Kuo Zhan, Yunzhe Jiang, Peng Qin, Yunlin Chen, and Lars Heinke*

The unambiguous detection and classification of volatile organic compounds (VOCs) are crucial in many fields. For using VOC-sensing to explore the alteration and spoilage of food, very inexpensive sensors are desired. Simple colorimetric sensors seem highly attractive for these applications. Here, a label-free, colorimetric sensor array made of metal-organic-framework-based (MOF-based) Fabry-Pérot (FP) films is presented where the signal read-out is performed either by their optical spectra or by pictures taken with a smartphone camera. Exposing the FP-MOF-films to various VOCs causes a reversible shift of the photonic pattern, where the magnitude of the shift depends on the VOC type, its concentration, and the MOF structure. The application of machine- learning- algorithms on the sensor data allows to identify the VOCs with a high classification accuracy (92% at 100 ppm). It is shown that the sensor array read-out can also be performed with a common smartphone camera, also precisely classifying the VOC analytes. Moreover, fresh and spoiled food, like milk and meat, is distinguished by its head space. Thus, the study presents a very inexpensive platform of small colorimetric sensors that allow determining the quality, alteration, and spoilage of food, and it may contribute to realizing smart labels and intelligent packaging.

1. Introduction

Food spoilage is usually correlated with the exposure of different molecules, which belong to the large group of volatile organic compounds (VOCs).[1–4] Often, the human olfactory system, i.e., our nose, can detect these VOCs and we can detect whether the food or drinks are eatable or rotten. Examples are rotten eggs that expose hydrogen sulfide (with a distinct odor) and spoiled milk that exposes VOCs like alcohols and acetone.[5,6] Consuming spoiled food may possess a severe health concern and it is estimated that thousands of people suffer illness and die annually due to the consumption of rotten food products.[7] Apart from the health concern and the individual misfortune that the food cannot be consumed, food spoilage presents severe (macro-)economic damage. It is estimated that roughly one-third of the food produced for humans is wasted, lost or spoils, which amounts to more than one billion tons of food every year.[8,9] The usage of expiration dates, use-by- and best-before-dates provides an orientation for the consumer when the food may (start to) spoil. However, using such an inflexible date (and the misinterpretation of the meaning) results in the disposal of significant amounts of edible food products.[10,11] As solution, smart labels and intelligent packaging that provide the consumer the information of the food spoilage are suggested (regardless of the expiration date), so that no unspoiled food is disposed.[12–14] This may save huge amounts of valuable resources. The key components of such smart labels are inexpensive sensors. The very low price of the sensors, which is fundamental for an economic application, excludes the usage of any technical signal transducer. Thus, an optical signal read-out, which can be performed by a common smartphone (that most people constantly carry with them), seems promising. Moreover, the sensor system must be stable, robust, and non-toxic.

Food spoilage often goes along with the exposure of VOCs and complex VOC mixtures. To identify the VOCs, the usage of sensor arrays is promising.[15,16] Ideally, the individual sensors in the array possess different affinities and selectivities, so that the data of the entire array allow the classification of the VOC or VOC mixture (although each sensor may have a low chemical specificity). In contrast to sensor arrays based on gravimetric transducers or conductance changes,[17–20] colorimetric sensor arrays do not require any extensive signal transduction setup.[21–24] Moreover, they can be minimized and are extremely energy-saving.[25]

K. Zhan, Y. Jiang, P. Qin, L. Heinke
Institute of Functional Interfaces (IFG)
Karlsruhe Institute of Technology (KIT)
76344 Eggenstein-Leopoldshafen, Germany
E-mail: Lars.Heinke@kit.edu
K. Zhan, Y. Chen
School of Physical Science and Engineering
Beijing Jiaotong University
Beijing 100044, China

Ideally, the colorimetric sensor arrays produce a composite pattern of colorimetric responses as a unique optical "fingerprint" for each analyte.[26] So far, colorimetric sensor arrays have focused on utilizing dyes and pigments as responsive materials, which are the labels probing the chemical reactivity of the analytes.[27–30] However, these labels operate typically not reversible, so repeatable sensing is not feasible. This is caused by the strong intermolecular interactions between the sensor labels and the analytes, often based on ionic bonding, covalent or coordination bond formation, and Brønsted or Lewis acid-base interactions.[31] To date, realizing a label-free, repeatable, and reversible colorimetric array-based sensor to detect and identify diverse analytes remains a significant challenge.

Apart from using responsive dye molecules, the color of a material can also be changed by photonic effects. A Fabry–Pérot (FP) cavity is a thin film with a thickness in the order of the wavelength of light between two parallel surfaces, (partially) reflecting the light.[32,33] The color of the FP cavity is controlled by the thickness and the optical density of the film. Since the uptake of guest molecules change the optical density, FP-films can also be used as colorimetric sensors.[34,35] Traditionally, FP-films are made of inorganic materials or polymers.[34,36] For applications as advanced sensors or sensor arrays, the FP-films should be made of diverse, highly porous materials with large specific surface areas, well-defined crystalline structures and designed chemically functionalities. Moreover, the materials need to be transparent. Thin films of metal–organic frameworks, MOFs,[37,38] are a material class which seems ideally suited for such tasks.[39–41] MOFs consist of metal nodes connected by organic ligand molecules. MOF possess many unique properties, such as high specific surface areas, very diversified structures and tailorable functionalities.[42] As a result, MOFs and MOF arrays were explored for various sensing applications.[43–46] For FP-based sensing, the MOF material needs to be prepared in the form of thin film. By making the MOF films in a layer-by-layer fashion, surface-mounted MOFs (SURMOFs) are prepared, which typically show a homogeneous morphology with a high degree of structural order and a low defect density.[47] To date, SURMOFs were used in gravimetric sensor arrays based on quartz crystal microbalance.[48–50] Moreover, SURMOFs and other MOF films were also used in photonic 1D crystals (Braggs stacks) sensors.[51–53] Single homogenous MOF films were also used as FP-cavity, where the refractive index (RI) increases with the VOC uptake, working as a single optical gas sensor.[54,55] However, since only single FP-sensors were used, different analytes (also at different concentrations) could not be discriminated. Colorimetric sensor arrays based on MOF-based FP-cavities have not yet been presented.

Here, we present colorimetric label-free sensor arrays based on MOF films in Fabry-Pérot (FP) cavities. The sensor arrays are made of MOF films with different structures, which are Zn-based MOFs (ZIF-8[56] and $Zn_2(BDC)_2(dabco)$[57,58]) and also extended by Cu-based MOFs (HKUST-1,[59] $Cu_2(BDC)_2(dabco)$[58] and $Cu_2(BDC)_2(BiPy)$[58,60]). (ZIF stands for zeolitic imidazolate framework, HKUST for Hong Kong University of Science and Technology, BDC for benzene-1,4-dicarboxylic acid (terephthalic acid), dabco for 1,4-diazabicyclo[2.2.2]octane and BiPy for 4,4′-bipyridine.). We chose popular MOF structures with a high porosity and a good thermal and chemical stability. The MOF pores are connected by a 3D pore system, allowing the fast mass transfer through the pores. Moreover, the synthesis procedure for preparing thin homogenous films of these MOFs with a low defect density are explored. Based on the two Zn-based SUR-MOFs, we constructed a non-toxic FP-MOF-sensor array. The colorimetric array in combination with UV–vis spectroscopy is able to reversibly detect various VOCs at low concentrations with limit of detections (LODs) in the order of 10–50 ppm. Using simple machine learning algorithms to analyze the data, the sensor array can distinguish the VOCs (methanol, ethanol, acetone, 1-propanol, *m*-xylene, and hexane) with very high classification accuracy. The sensor array works fully reversible with response and recovery times of less than 1 min. Even more important, avoiding lab equipment and using only the digital camera of a common smartphone also allows to detect and classify the different VOCs precisely. We demonstrate that taken pictures of the colorimetric sensor array allows to explore the spoilage of food, classifying unspoiled and spoiled milk. In addition to the Zn-based-MOF arrays, the concept was also demonstrated for Cu-based-MOFs, where it was used to detect and discriminate various VOCs and to classify the spoilage of meat products.

2. Experimental Section

2.1. Synthesis of FP-SURMOF Films

The SURMOF films were prepared in a layer-by-layer fashion, as outlined in **Figure 1**. The substrates (silicon with native silicon oxide for ZIF-8 and 11-mercapto-1-undecanol-functionalized gold thin film on silicon for $Zn_2(BDC)_2(dabco)$ and for the Cu-based MOFs) were alternatively immersed in the ethanolic solutions of the metal nodes and of the linker molecules, see Supporting Information. The metal nodes were $Zn(NO_3)_2 \cdot 6H_2O$ or $Cu(CH_3COO)_2 \cdot H_2O$ with a concentration of 0.2 mM. The linker molecules were 2-methylimidazole (for ZIF-8), BDC and dabco (for $Zn_2(BDC)_2(dabco)$), BTC (trimesic acid for HKUST-1), BDC and dabco (for $Cu_2(BDC)_2(dabco)$), and BDC and BiPy (for $Cu_2(BDC)_2(BiPy)$) with a concentration of 0.1 mM. The syntheses were performed with a dipping robot[61] with 50 cycles each. On top of the MOF films, platinum films of ≈2 nm thickness were sputtered by a Sputter Coater MED020. The Pt film acts as a mirror, resulting in the FP-film.

2.2. Sample Characterization

X-ray diffraction (XRD) analysis was performed using a Bruker D8-Advance diffractometer with a Bragg-Brentano (θ–θ) geometry with a wavelength of $\lambda = 0.154$ nm. The (111) peak of the gold substrate was used as a reference, verifying the correct sample height.

UV–vis reflection spectra were recorded with an Agilent Cary 5000 spectrometer and UMA unit. The wavelength resolution was set to 0.1 nm. The spectra were recorded in reflectance with an angle of 30° to the surface normal. The position of the reflectance peak wavelength was determined by fitting a Gaussian function to the data in a range of ≈20 nm. In addition to the evaluation of the wavelength of the reflectance peak as sensor signal, the intensity of the reflectance peak (in a range of 5 nm around
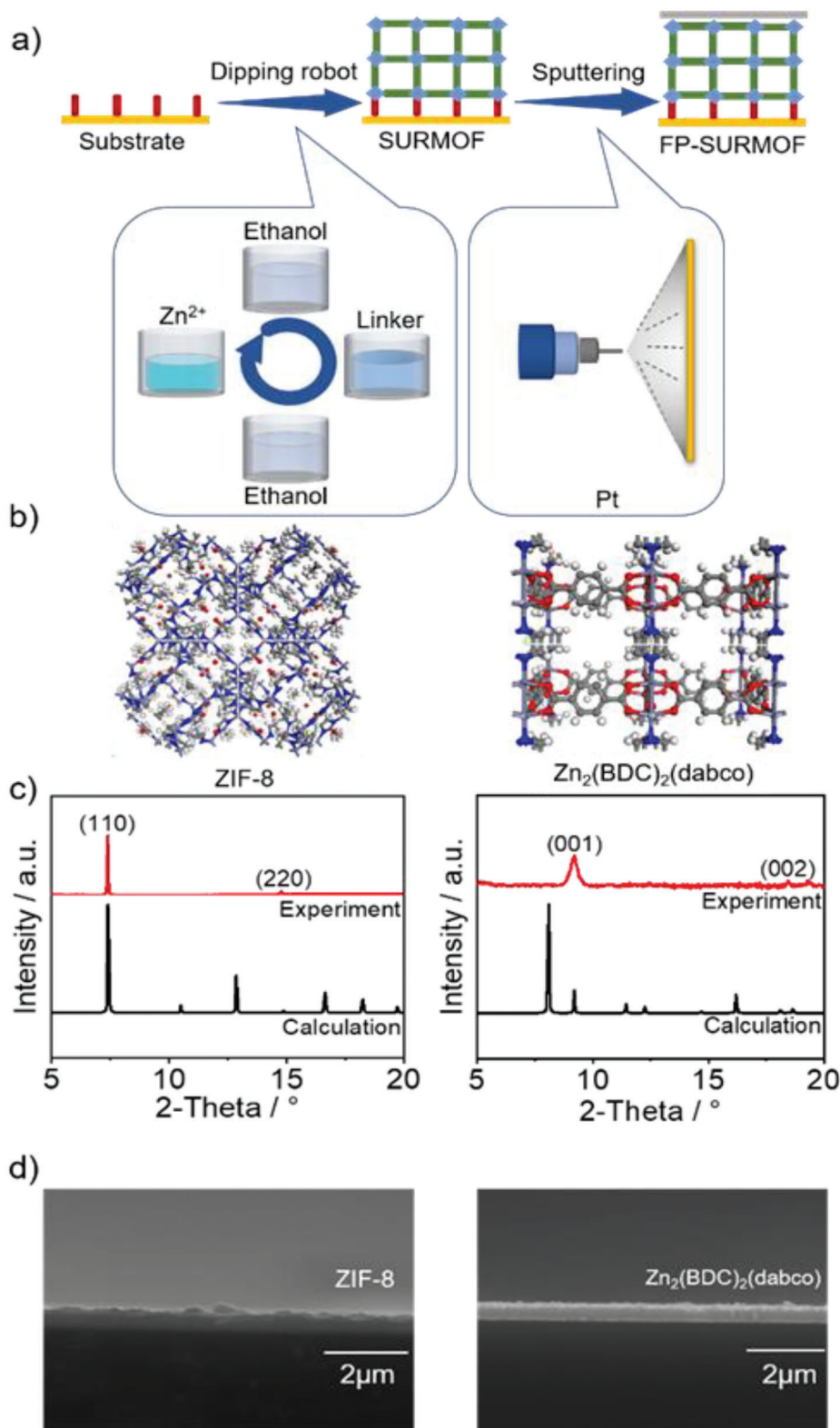
2300329 (2 of 10)

**ADVANCED
SCIENCE NEWS**

www.advancedsciencenews.com

**ADVANCED
MATERIALS
INTERFACES**
Open Access

www.advmatinterfaces.de

Figure 1. a) The fabrication process of the FP-SURMOF-sensors. b) Sketches of the MOF structures, see labels. c) X-ray diffractograms of the ZIF-8 film (left) and of the $Zn_2(BDC)_2(dabco)$ film (right). The X-ray wavelength is 0.154 nm. The experimental data are in red, and the patterns calculated for the targeted structure are shown in black. The experimentally observed diffraction peaks are labeled. d) SEM images of the ZIF-8 film (left) and of the $Zn_2(BDC)_2(dabco)$ film (right). The cross-sections of the broken sample are shown.

2300329 (3 of 10)

**ADVANCED
SCIENCE NEWS**

www.advancedsciencenews.com

**ADVANCED
MATERIALS
INTERFACES**

www.advmatinterfaces.de

the reflectance peak maximum) was also tested as a sensor response.

Infrared spectral analysis was performed with a Fourier Transform Infrared Reflection Absorption Spectrometer Bruker VERTEX 80. The spectra were recorded with an incidence angle of 80° with respect to the normal.

Scanning electron microscopy (SEM) images were recorded with a TESCAN VEGA3 tungsten heated filament scanning electron microscope. The samples were coated with a thin Pt film to avoid charging effects. The sample was imaged under high vacuum conditions and using an acceleration voltage of 20 kV.

2.2.1. VOC Exposure

The samples were located inside a cuvette with a gas in/out tube system. The gas flow inside the cuvette was controlled by two mass flow controllers (MFCs). The gas stream of the carrier gas (nitrogen) was divided into two streams, one stream provides a constant nitrogen flow of 300 mL min^{-1}. The other stream passes through the wash bottle filled with the VOC-liquids to produce a VOC-enriched vapor stream with a vapor pressure slightly smaller than the saturated vapor pressure. Both gas streams were combined with fixed flow rates, controlling the partial pressure in the final gas stream.

2.2.2. Sensor Setup for Taking Pictures with the Phone Camera

The sensors were placed in a sealed transparent Petri dish with a gas flow going in and out (via tubes). An iPhone XR, fixed at a distance of 40 cm with an angle perpendicular to the sample surface, was used to take the photos.

2.2.3. Exposure to Milk and Meat Headspace

The milk samples ($\approx$20 mL) were stored in bottles (100 mL) and kept in the fridge ($\approx$275 K) or in the lab at room temperature ($\approx$295 K), respectively. The beef meat sample ($\approx$5 g) was stored in a bottle (100 mL) at room temperature. For the sensing, a stream of nitrogen flows through the bottles and then passes the sensor's chamber.

All experiments were performed at room temperature.

2.3. Data Analyses

Data analysis and classification were performed using standard k-nearest neighbor (kNN), Support Vector Machine (SVM), and Artificial Neural Network (ANN) machine learning algorithms via program codes written in Python 3 and performed in the open-source platform Jupyter notebook. For the spectra kNN, SVM, and ANN classification, a total of 50 data points of the intensity value at the reflectance peak (5 nm around the reflectance peak with the highest reflectance with a resolution of 0.1 nm) were collected before and under the vapor exposure. Each data point for analysis includes the reflectance intensities of both two FP-MOF-film, thus each data point is a 2D vector. A total of 350 data points

were collected for the pristine sample and six odors (each for 50 points). The K value in kNN was set to 18 (which is close to the square root of 350). The kernel function in SVM was set to linear function. The hidden layer sizes in ANN were set to ten. The data were classified using five-fold cross validation, where 80% of the data points (i.e., 280 points) were used as the training set and 20% were used as the test set (i.e., 70 points).

For the kNN analysis of the photo-RGB data, a total of ten data points of the RGB values of the photos were collected before and after the vapor exposure. Each data point includes the three RGB values of both two FP-MOF-film, thus each data point is a six-dimensional vector. A total of 70 data points for analysis were collected (for the pristine sample and the six odors). The K value in kNN was set to eight (which is close to the square root of 70). The data were classified using five-fold cross validation, where 80% of the data points (i.e., 56 points) were used as the training set and 20% were used as the test set (14 points).

The outcome of the kNN, SVM, and ANN algorithm was the grouping of the data to the different classes and the comparison if the assignments to the classes were correct or wrong, shown in the confusion matrix. The used KNN and ANN program code is given in in Refs. [49,50]. The used SVM program code is given in the Supporting Information.

3. Results and Discussion

The MOF films were prepared in a layer-by-layer fashion directly on the substrate, resulting in surface-mounted MOFs, SURMOFs, Figure 1a. On top of the SURMOFs, a very thin layer of platinum (with a nominal thickness of 2 nm) was sputtered, which is reflecting but not dense, allowing guest molecules to penetrate. First, we focus on MOFs with ZIF-8 and $Zn_2(BDC)_2(dabco)$ structures, Figure 1b. The crystallinity of the SURMOF films was explored by X-ray diffraction (XRD). The XRD data show that both samples are crystalline, and their structures correspond to the targeted MOFs, Figure 1c. The samples are further characterized by infrared reflection absorption spectroscopy (IRRAS, Figure S1, Supporting Information), verifying the composition of the MOF structures. The SEM images, in Figure 1d, show that the samples have a homogeneous morphology with a small surface roughness. The cross-section images show that both SURMOF films are $\approx$500 nm thick.

The reflection spectra and their corresponding CIE chromaticity coordinates for the pristine (unloaded) FP-SURMOF films are presented in Figure S2 (Supporting Information). The FP-ZIF-8 film shows values of CIEx = 0.269 and CIEy = 0.338. The FP-$Zn_2(BDC)_2(dabco)$ film shows values of CIEx = 0.429 and CIEy = 0.408.

The sensing performance of the Zn-based FP-SURMOFs array was tested for six VOCs as analytes. The VOCs comprise acetone (Ace), methanol (MeOH), ethanol (EtOH), 1-propanol (PrOH), *m*-xylene (*m*-Xy), and hexane (Hex), see **Table 1**. The UV–vis spectra of the FP-SURMOF films in a controlled VOC atmosphere were recorded in reflection. The reflectance spectra of the FP-ZIF-8 and FP-$Zn_2(BDC)_2(dabco)$ films, either empty (pristine) or exposed to the saturated VOC vapors, are shown in **Figure 2**a and Figure S8 (Supporting Information), respectively. (The vapor pressures of the saturated vapors are given in Table 1.) The spectra show that the pristine FP-SURMOF films have the

ADVANCED
SCIENCE NEWS

www.advancedsciencenews.com

ADVANCED
MATERIALS
INTERFACES
Open Access

www.advmatinterfaces.de

Table 1. Sensor parameters of the FP-SURMOF films.

	FP-SURMOF film	Wavelength sensitivity in nm/ppm	Wavelength-LOD in ppm	Intensity sensitivity in %/ppm	Intensity-LOD in ppm
Ace (acetone) p_{sat} = 24 kPa	ZIF-8	4.3×10^{-3}	11.2	-4.9×10^{-3}	12.9
	$Zn_2(BDC)_2(dabco)$	5.7×10^{-3}	9.5	-5.6×10^{-3}	12.9
MeOH (methanol) p_{sat} = 16.67 kPa	ZIF-8	8.0×10^{-3}	6	-7.9×10^{-3}	8
	$Zn_2(BDC)_2(dabco)$	6.7×10^{-3}	8.1	-6.2×10^{-3}	11.6
EtOH (ethanol) p_{sat} = 7.96 kPa	ZIF-8	6.3×10^{-3}	7.6	-6.3×10^{-3}	10
	$Zn_2(BDC)_2(dabco)$	8.7×10^{-3}	6.2	-8.1×10^{-3}	8.9
PrOH (1-propanol) p_{sat} = 2.78 kPa	ZIF-8	5.3×10^{-3}	9.2	-5.5×10^{-3}	11.5
	$Zn_2(BDC)_2(dabco)$	5.3×10^{-3}	10.2	-5.4×10^{-3}	13.3
m-Xy (m-xylene) p_{sat} = 1.33 kPa	ZIF-8	0.9×10^{-3}	54.4	-1.2×10^{-3}	52.5
	$Zn_2(BDC)_2(dabco)$	1.0×10^{-3}	54	-1.3×10^{-3}	55.4
Hex (hexane) p_{sat} = 17 kPa	ZIF-8	1.5×10^{-3}	32	-1.5×10^{-3}	42
	$Zn_2(BDC)_2(dabco)$	1.9×10^{-3}	28.4	-1.8×10^{-3}	40

strongest reflectance peaks at 475.5 nm with a reflectance intensity of 45.67% for ZIF-8 and at 476.6 nm with an intensity of 48.90% for $Zn_2(BDC)_2(dabco)$, respectively.

The reflectance spectra of the FP-ZIF-8 film and the FP-$Zn_2(BDC)_2(dabco)$ film under the exposure to VOCs with small vapor concentrations (100-400 ppm) are shown in Figures S4–S7 (Supporting Information). Upon analyte exposure, the spectra show a shift of the position and of the intensity of the re-

flectance peak. The wavelength shift of the strongest reflectance peak versus the vapor pressure of the different analytes are shown in Figure 2b and Figure S8 (Supporting Information). Both FP-SURMOF films show linear dependences of the wavelength shift of the reflectance peak and the VOC vapor concentration (0–400 ppm), however, the proportionality factor, which is the wavelength sensitivity (i.e., the slope in Figure 2b) varies. The wavelength sensitivity data are given in Table 1.
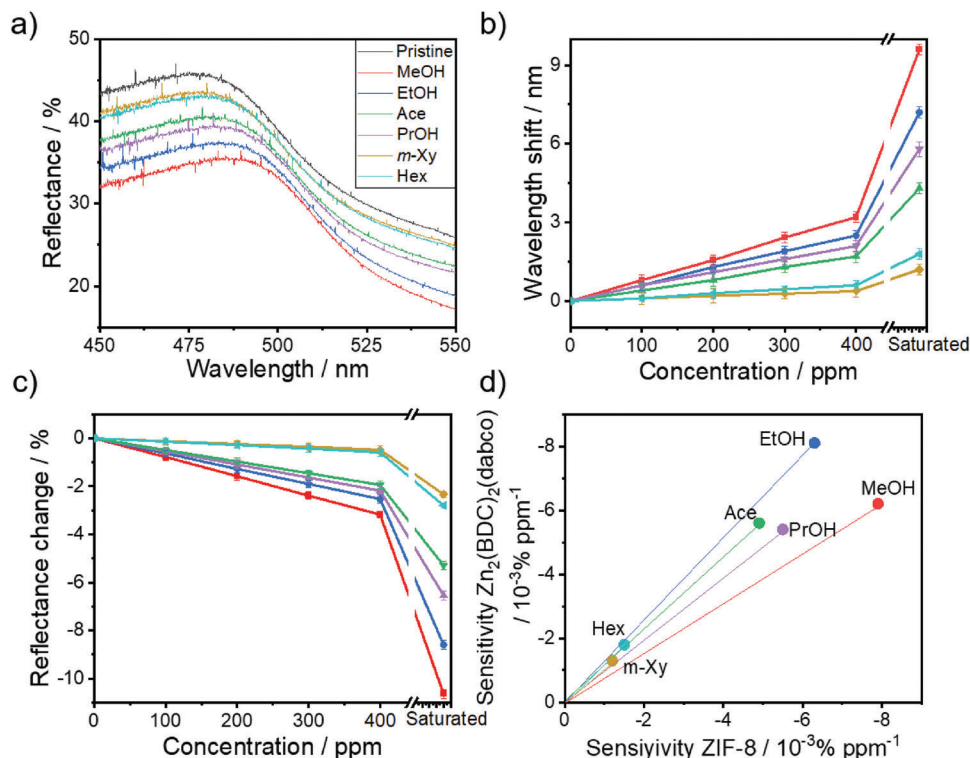

Figure 2. a) The reflectance spectra of the FP-ZIF-8 film in the atmosphere of saturated VOCs, see labels (the same colors represent the same VOC analytes in all panels). b) The wavelength shift of the strongest reflectance peak of the FP-ZIF-8 film in different VOC vapors with different concentrations. c) The intensity change of the strongest reflectance peak of the FP-ZIF-8 film in different VOC vapors with different concentrations. The entire UV–vis spectra as well as the corresponding data for the FP-$Zn_2(BDC)_2(dabco)$-film are shown in Figures S6–S8 (Supporting Information). d) 2d-plot of the intensity sensitivity (see panel c) in the sensors. The analytes are labeled.
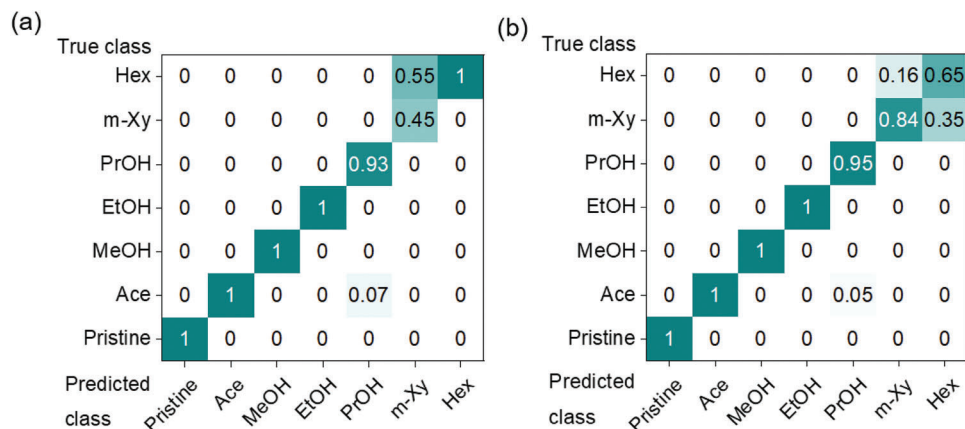
Figure 3. The confusion matrix for the classification of the six VOCs at a concentration of 100 ppm and the pristine (empty) state. Analyzed by a) SVM and b) kNN. The true classes are the rows, and the predicted classes are the columns.

The changes of the intensity of the strongest reflectance peak versus the vapor pressure of the different analytes are shown in Figure 2c. Like the wavelength shift, both FP-SURMOF films show linear dependences of the intensity change of the reflectance peak and the VOC vapor concentration. Here, the proportionality factor (i.e., the slope in Figure 2c and Figure S8, Supporting Information) is termed intensity sensitivity, which also depends on the VOC type and MOF. The intensity sensitivity data are given in Table 1. Comparing Figure 2b,c shows that the shift of the reflectance intensity and of the reflectance wavelength are very similar (but with opposite signs).

The limits of detection (LODs) were calculated by the sensitivity divided by three times the standard deviation, following general recommendations.[62,63] The wavelength standard deviation was determined by the variation of the peak position of the pristine sample in three subsequent measurements. (The values are 0.016 and 0.018 nm for the FP-ZIF-8 and the FP-$Zn_2(BDC)_2$(dabco) sample, respectively.). The calculated LODs for the different VOCs based on the wavelength shift, referred to as wavelength-LODs, are shown in Table 1. The standard deviation of the reflectance intensity was determined in three subsequent measurements. (The values are 0.021% for FP-ZIF-8 and 0.024% for FP-$Zn_2(BDC)_2$(dabco) sample.) The LODs based on
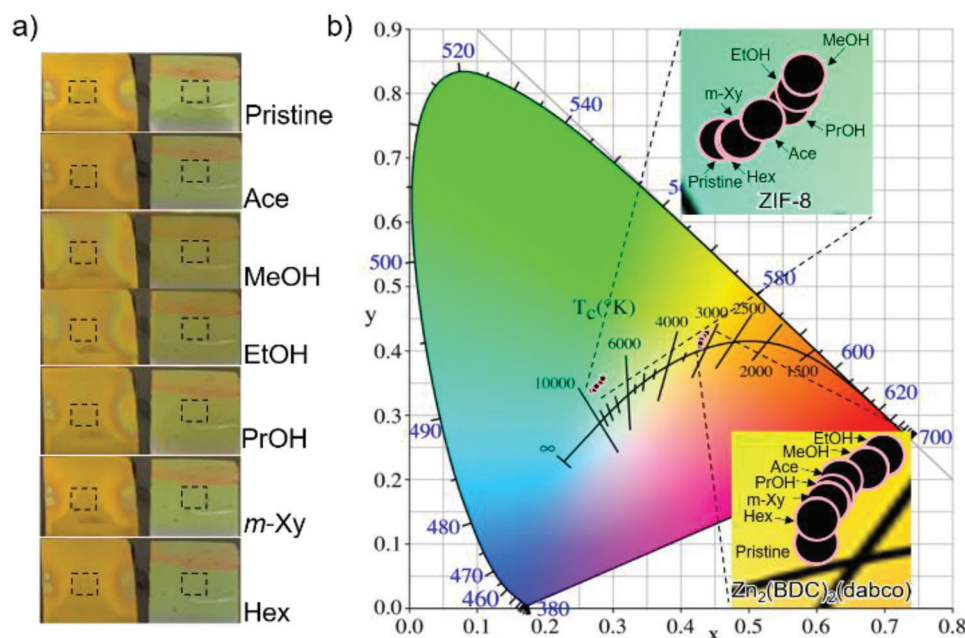

Figure 4. a) Photos of the sensor array, either in pure nitrogen (pristine) or in saturated VOC vapors, see labels. (The dotted rectangles with a size of 2.5 mm × 3 mm present the area where the RGB values were determined.) Right-hand side: FP-ZIF-8 film; left-hand side: FP-$Zn_2(BDC)_2$(dabco) film. b) CIE-color-space diagram with the RGB values of the FP-SURMOF sensors in saturated VOC vapors. The insets are magnifications to show changes in the sensor RGB value.

**ADVANCED
SCIENCE NEWS**

www.advancedsciencenews.com

**ADVANCED
MATERIALS
INTERFACES**
Open Access

www.advmatinterfaces.de

the reflectance-intensity-change, referred to as intensity-LOD, are also shown in Table 1. Noteworthy, the LODs determined via both methods are similar for the same analyte. The LODs of both MOF samples are in the range of 6 to 55 ppm for all explored analytes, significantly smaller than 100 ppm. (This is in line with the very high classification accuracy of the different VOCs at 100 ppm, see below.)

The repeatability is explored by repeating the VOC expose experiments, Figure S8 (Supporting Information). The data show that the sensor exposure is fully reversible and repeatable, as a result of the reversible VOC uptake by and release from the SUR-MOF film.

Both sensors show different sensitivities (both, wavelength and intensity sensitivities) for the same VOC vapor and different VOCs exhibit different sensitivities in the same sensor, Figure 2d and Table 1. This means, in the sensor array data, each analyte has a characteristic vector (where the components are the intensity change of the reflectance peak in ZIF-8 and $Zn_2(BDC)_2(dabco)$). This vector is like the fingerprint of the VOC, allowing its discrimination, see Figure 2d.

For determining the accuracy of the sensor array to discriminate the VOCs, we analyzed the data with simple machine learning algorithms. To this end, we apply three classification machine learning algorithms that are k-Nearest Neighbor (kNN), Support Vector Machine (SVM), and Artificial Neural Network (ANN) to identify the analytes based on the sensor data.[49,50] The accuracies of the data classification are shown in the confusion matrix, in **Figure 3**. Correct classifications are shown on the matrix's main diagonal; misclassifications are the other values. Figure 3a shows the quantitative identifications of VOCs at 100 ppm by SVM, indicating a correct identification with an average classification accuracy of 91.1%. The kNN analysis, Figure 3b, shows similar, also very good results with a slightly higher average classification accuracy of 92.0%. Confusion matrices by the ANN analysis as well as from other concentrations (200, 300, 400 ppm, and saturated VOCs) are shown in Figures S9–S11 (Supporting Information). All results show very high classification accuracies, demonstrating the sensor array of ZIF-8 and $Zn_2(BDC)_2(dabco)$ FP-films allows the classification of the six tested VOCs. Generally, a higher VOC concentration results in higher classification accuracies, and a classification accuracy of 100% was reached for a vapor pressure of 400 ppm and for saturated vapor pressure.

Noteworthy, the FP-SURMOF sensors show significant wavelength and intensity shifts of the reflectance peaks, which go along with the change of color. To employ the color changes for the sensor performance, we place the FP-SURMOF sensors next to each other and take pictures of the sensor array with the digital camera of a common smartphone (here we use an iPhone XR). From the pictures (without color balance), the RGB values were used as the sensor signal. Although the color changes are not tremendous, the RGB values change significantly upon analyte exposure, see Tables S1 and S2 (Supporting Information). For example, the RGB values of the pristine $Zn_2(BDC)_2(dabco)$ SURMOF changes from (197,155,35) to (160,124,32) upon the ethanol exposure.

The RGB data were analyzed by the machine learning algorithms to recognize and classify the six VOCs. **Figure 4**a shows the photos of the FP-SURMOF films in the different VOC atmospheres. The RGB values of the sensors are shown in the
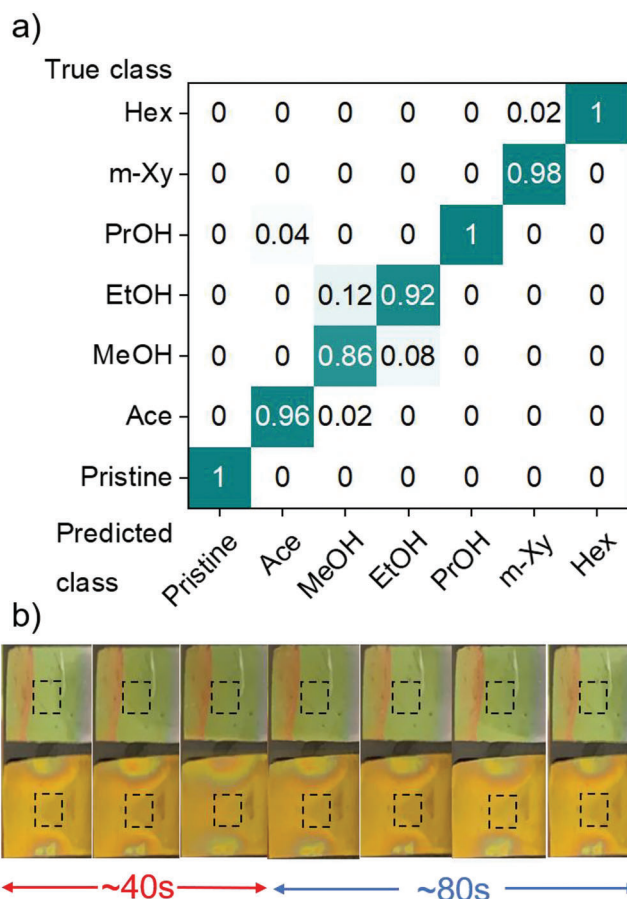

Figure 5. a) The kNN confusion matrix for the classification of the six VOCs with a saturated vapor pressure and the pristine sample. b) Photos of the sensor array in saturated MeOH vapor (three images left, red arrow) and afterward in pure nitrogen (five images right, blue arrow). The time between each image is ≈20 s. The dotted rectangles with a size of 2.5 mm × 3 mm present the area where the RGB values are determined.

CIE-color-space diagram in Figure 4b. It shows that the color of the sensor changes with the VOC exposure. This means the FP-SURMOF films show a colorimetric sensor response, where the sensor response depends on the analyte. The RGB values of the sensor array are shown in Table S1 (Supporting Information).

Analyzing the RGB data of the sensors shows that different VOCs can be classified very well, **Figure 5**a. The average classification accuracy by using the kNN algorithm is 96.0% for the saturated VOC vapors. Please note, this value is somewhat smaller than the classification accuracy by using the UV–vis spectra (Figure S7d, Supporting Information, 100%), but the value is still large enough to precisely determine each VOC. The response and recovery time are explored in Figure 5b and Figure S28 (Supporting Information). The data show that ≈40 s after the beginning of the exposure to the VOC (here methanol), a stable picture with stable RGB values is obtained. For the release of the VOC, after ≈80 s, the RGB values of the sensors are stable and coincide with the values of the pristine sensor. The transient change of the RGB values during VOC exposure is shown in Figure S28 (Supporting Information), verifying the estimated response time.
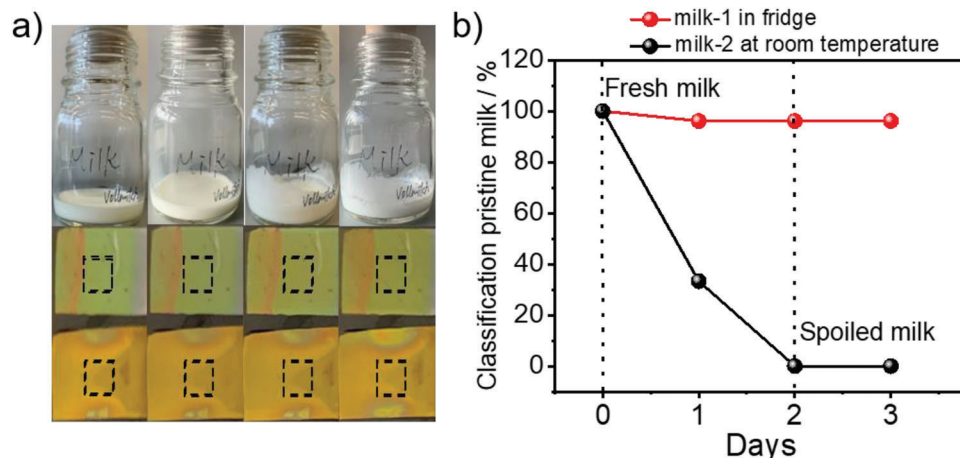
**ADVANCED
SCIENCE NEWS**

www.advancedsciencenews.com

**ADVANCED
MATERIALS
INTERFACES**

Open Access

www.advmatinterfaces.de

Figure 6. a) Photos of the milk-2 (at room temperature, ≈295 K) in a bottle for three days (left to right: day 0 to 3rd day) with corresponding photos of the sensor array. The dotted rectangles with a size of 2.5 mm × 3 mm present the area where the RGB values are determined. b) The accuracy of classifying the milk as pristine, unspoiled milk for the aging samples.

We continue and show that the FP-SURMOF sensor array in combination with the smartphone camera can be used for practical applications. We used it to detect the spoilage of milk, which usually goes along with the exposure of VOCs like acetone and alcohols.[5,6,12] To this end, we exposed the sensor array to the vapor of the milk. We compare two milk samples: While one sample was kept in the refrigerator (≈275K, milk-1), the other sample was kept at room temperature (≈295K, milk-2). The data, which means the RGB values of the images taken with the smart phone, were analyzed by kNN. **Figure 6**a shows the milk and the sensor array. The RGB values and the confusion matrices of the analysis are shown in Table S2 and Figure S12 (Supporting Information), respectively. Most important, Figure 6b shows the accuracy of classifying the milk as pristine milk, i.e., unspoiled milk. While the refrigerated milk shows no change of the sensor response, the non-refrigerated milk shows a change of the sensor response. After one day, the sensor signal has only a small overlap with the pristine signal (of ≈40%) and from the 2nd day on (after 48 h), the sensor signal has no overlap with the pristine milk and its headspace is classified as fully different (i.e., fully different from pristine, unspoiled milk). We term the altered milk as "spoiled". This is in line with a slight smell of spoiled milk that was perceived by us.

For demonstrating that the concept of using MOF films in such FP-sensor is not limited to the presented Zn-based MOFs, we prepared a FP-SURMOF sensor array based on HKUST-1, $Cu_2(BDC)_2(dabco)$ and $Cu_2(BDC)_2(BiPy)$. The data, Figures S14–S32 (Supporting Information), show that the sensor array is able to detect and classify six different VOCs. The LODs are ≈19 to ≈41 ppm and the classification accuracy at 100 ppm is 96.7% by kNN. The sensor array was applied to explore and unveil the spoilage of meat. It shows that the sensor array is able to classify pristine and spoiled meat by its vapor (head space). In this way, the spoilage of the food product was observed.

We would like to stress that the core component here, i.e., the MOF structures, are very cheap and can be made in large scale areas.[64] In the future, the substrate and top-mirror materials (which is here made of rather expensive materials like Si, Pt, and Au) will be substituted by cost-efficient polymeric materials.[65,66] In practical (future) applications, the sensor production must also be standardized resulting in films with minor deviations of the thickness (below 1 nm) or each sensor needs to be calibrated.

4. Conclusion

We developed a label-free, inexpensive, and reversible colorimetric FP-SURMOFs sensor array. Here, the sensors are based either on non-toxic Zn-based MOF structure or on Cu-based MOFs. The data can be analyzed either by UV–vis spectroscopy (using laboratory equipment) or by the digital camera of a smart phone, avoiding lab equipment. The FP-SURMOF sensors show a high sensitivity, low LOD in the range of ≈10–50 ppm and excellent repeatability for various VOCs. By using the smartphone as analysis device, a classification accuracy of over 90% was realized for six tested VOCs. Moreover, the sensor device can be used to detect food spoilage, demonstrated for milk and meat.

This work shows a very inexpensive platform of very small, portable, and label-free colorimetric sensors that allows determining the quality, alteration, and spoilage of food. We foresee that various MOF structures, going far beyond the Zn- and Cu-based MOFs, can be used in such FP-based sensor arrays, also including edible MOFs.[67] In that way, it may contribute to realize simple and versatile sensors, smart labels and intelligent packaging. Such versatile sensors can be used in food quality assurance and will realize safer groceries, but also may find application in agriculture, pollution monitoring, and medical diagnosis.

Supporting Information

Supporting Information is available from the Wiley Online Library or from the author.

[1] W. Liszkowska, J. Berlowska, *Molecules* **2021**, *26*, 1035.
[2] N.-T. Phan, K.-H. Kim, E.-C. Jeon, U.-H. Kim, J. R. Sohn, S. K. Pandey, *Environ. Monit. Assess.* **2012**, *184*, 1683.
[3] Y. Xu, W. Cheung, C. L. Winder, R. Goodacre, *Anal. Bioanal. Chem.* **2010**, *397*, 2439.
[4] S. Panigrahi, S. Sankaran, S. Mallik, B. Gaddam, A. A. Hanson, *Mater. Sci. Eng., C* **2012**, *32*, 1307.
[5] M. Decimo, M. C. Cabeza, J. A. Ordóñez, I. De Noni, M. Brasca, *Int. J. Dairy Technol.* **2018**, *71*, 593.
[6] P. Silcock, M. Alothman, E. Zardin, S. Heenan, C. Siefarth, P. Bremer, J. Beauchamp, *Food Packag. Shelf Life* **2014**, *2*, 81.
[7] W. H. Organization, in *Food Safety: What You Should Know*, World Health Organization, Geneva **2015**.
[8] Q. D. Read, M. K. Muth, *Resour., Conserv. Recycl.* **2021**, *168*, 105448.
[9] K. Silvennoinen, J.-M. Katajajuuri, H. Hartikainen, L. Heikkilä, A. Reinikainen, *Br. Food J.* **2014**.
[10] A. M. Barone, J. Aschemann-Witzel, *Food Control* **2022**, *133*, 108615.
[11] K. Schmidt, *Food Qual. Prefer.* **2019**, *78*, 103746.
[12] S. Matindoust, M. Baghaei-Nejad, M. H. S. Abadi, Z. Zou, L.-R. Zheng, *Sens. Rev.* **2016**, *36*, 169.
[13] H. Yousefi, H.-M. Su, S. M. Imani, K. Alkhaldi, C. D. M. Filipe, T. F. Didar, *ACS Sens.* **2019**, *4*, 808.
[14] K. Biji, C. Ravishankar, C. Mohan, T. Srinivasa Gopal, *J. Food Sci. Technol.* **2015**, *52*, 6125.
[15] L. Spinelle, M. Gerboles, G. Kok, S. Persijn, T. Sauerwald, *Sensors* **2017**, *17*, 1520.
[16] F. Röck, N. Barsan, U. Weimar, *Chem. Rev.* **2008**, *108*, 705.
[17] S. Fanget, S. Hentz, P. Puget, J. Arcamone, M. Matheron, E. Colinet, P. Andreucci, L. Duraffourg, E. Myers, M. Roukes, *Sens. Actuators, B* **2011**, *160*, 804.
[18] A. Oprea, U. Weimar, *Anal. Bioanal. Chem.* **2019**, *411*, 1761.
[19] M. Hartwig, R. Zichner, Y. Joseph, *Chemosensors* **2018**, *6*, 66.
[20] M. Ehsani, P. Rahimi, Y. Joseph, *Sensors* **2021**, *21*, 3291.
[21] R. N. Dsouza, U. Pischel, W. M. Nau, *Chem. Rev.* **2011**, *111*, 7941.
[22] L. You, D. Zha, E. V. Anslyn, *Chem. Rev.* **2015**, *115*, 7840.
[23] J. R. Askim, M. Mahmoudi, K. S. Suslick, *Chem. Soc. Rev.* **2013**, *42*, 8649.

[24] X. Chen, Y. Zhou, X. Peng, J. Yoon, *Chem. Soc. Rev.* **2010**, *39*, 2120.
[25] K. S. Suslick, *Curr. Opin. Chem. Biol.* **2012**, *16*, 557.
[26] H. Lin, M. Jang, K. S. Suslick, *J. Am. Chem. Soc.* **2011**, *133*, 16786.
[27] C. A. Hunter, *Angew. Chem., Int. Ed.* **2004**, *43*, 5310.
[28] N. A. Rakow, K. S. Suslick, *Nature* **2000**, *406*, 710.
[29] Q. Chen, A. Liu, J. Zhao, Q. Ouyang, *J. Pharm. Biomed. Anal.* **2013**, *84*, 77.
[30] X. Zhong, D. Huo, H. Fa, X. Luo, Y. Wang, Y. Zhao, C. Hou, *Sens. Actuators, B* **2018**, *274*, 464.
[31] M. El-Desouki, M. J. Deen, Q. Fang, L. Liu, F. Tse, D. Armstrong, *Sensors* **2009**, *9*, 430.
[32] M. Islam, M. M. Ali, M.-H. Lai, K.-S. Lim, H. Ahmad, *Sensors* **2014**, *14*, 7451.
[33] J. P. Carmo, R. P. Rocha, M. Bartek, G. de Graaf, R. F. Wolffenbuttel, J. H. Correia, *Opt. Laser Technol.* **2012**, *44*, 2312.
[34] S. Khan, S. Le Calvé, D. Newport, *Sens. Actuators, A* **2020**, *302*, 111782.
[35] R. Kanawade, A. Kumar, D. Pawar, D. Late, S. Mondal, R. K. Sinha, *J. Opt. Soc. Am. B* **2019**, *36*, 684.
[36] M. Shaygan, Z. Wang, M. S. Elsayed, M. Otto, G. Iannaccone, A. H. Ghareeb, G. Fiori, R. Negra, D. Neumaier, *Nanoscale* **2017**, *9*, 11944.
[37] H. Furukawa, K. E. Cordova, M. O'Keeffe, O. M. Yaghi, *Science* **2013**, *341*, 1230444.
[38] S. Kaskel, in *The Chemistry of Metal-Organic Frameworks, 2 Volume Set: Synthesis, Characterization, and Applications*, John Wiley & Sons, New York **2016**.
[39] I. Stassen, N. Burtch, A. Talin, P. Falcaro, M. Allendorf, R. Ameloot, *Chem. Soc. Rev.* **2017**, *46*, 3185.
[40] E. Virmani, J. M. Rotter, A. Mähringer, T. Von Zons, A. Godt, T. Bein, S. Wuttke, D. D. Medina, *J. Am. Chem. Soc.* **2018**, *140*, 4812.
[41] P. Falcaro, R. Ricco, C. M. Doherty, K. Liang, A. J. Hill, M. J. Styles, *Chem. Soc. Rev.* **2014**, *43*, 5513.
[42] S. Kitagawa, *Chem. Soc. Rev.* **2014**, *43*, 5415.
[43] A. Chidambaram, K. C. Stylianou, *Inorg. Chem. Front.* **2018**, *5*, 979.
[44] S. K. Bhardwaj, N. Bhardwaj, R. Kaur, J. Mehta, A. L. Sharma, K.-H. Kim, A. Deep, *J. Mater. Chem. A* **2018**, *6*, 14992.
[45] M. Woellner, S. Hausdorf, N. Klein, P. Mueller, M. W. Smith, S. Kaskel, *Adv. Mater.* **2018**, *30*, 1704679.
[46] F.-Y. Yi, D. Chen, M.-K. Wu, L. Han, H.-L. Jiang, *Chempluschem* **2016**, *81*, 675.
[47] L. Heinke, C. Wöll, *Adv. Mater.* **2019**, *31*, 1806324.
[48] S. Okur, P. Qin, A. Chandresh, C. Li, Z. Zhang, U. Lemmer, L. Heinke, *Angew. Chem., Int. Ed.* **2021**, *60*, 3566.
[49] P. Qin, S. Okur, C. Li, A. Chandresh, D. Mutruc, S. Hecht, L. Heinke, *Chem. Sci.* **2021**, *12*, 15700.
[50] P. Qin, B. A. Day, S. Okur, C. Li, A. Chandresh, C. E. Wilmer, L. Heinke, *ACS Sens.* **2022**, *7*, 1666.
[51] Z. Zhang, K. Müller, S. Heidrich, M. Koenig, T. Hashem, T. Schlöder, D. Bleger, W. Wenzel, L. Heinke, *J. Phys. Chem. Lett.* **2019**, *10*, 6626.
[52] J. Liu, E. Redel, S. Walheim, Z. Wang, V. Oberst, J. Liu, S. Heissler, A. Welle, M. Moosmann, T. Scherer, *Chem. Mater.* **2015**, *27*, 1991.
[53] F. M. Hinterholzinger, A. Ranft, J. M. Feckl, B. Rühle, T. Bein, B. V. Lotsch, *J. Mater. Chem.* **2012**, *22*, 10356.
[54] G. Lu, J. T. Hupp, *J. Am. Chem. Soc.* **2010**, *132*, 7832.
[55] H.-T. Kim, W. Hwang, Y. Liu, M. Yu, *Opt. Express* **2020**, *28*, 29937.
[56] K. S. Park, Z. Ni, A. P. Côté, J. Y. Choi, R. Huang, F. J. Uribe-Romo, H. K. Chae, M. O'Keeffe, O. M. Yaghi, *Proc. Natl. Acad. Sci. USA* **2006**, *103*, 10186.
[57] D. N. Dybtsev, H. Chun, K. Kim, *Angew. Chem., Int. Ed.* **2004**, *116*, 5143.
[58] O. Shekhah, *Materials* **2010**, *3*, 1302.
[59] S. S.-Y. Chui, S. M.-F. Lo, J. P. Charmant, A. G. Orpen, I. D. Williams, *Science* **1999**, *283*, 2050.

[60] B. D. McCarthy, T. Liseev, A. M. Beiler, K. L. Materna, S. Ott, *ACS Appl. Mater. Interfaces* **2019**, *11*, 38294.

[61] Z.-G. Gu, A. Pfriem, S. Hamsch, H. Breitwieser, J. Wohlgemuth, L. Heinke, H. Gliemann, C. Wöll, *Microporous Mesoporous Mater.* **2015**, *211*, 82.

[62] A. J. deMello, *ACS Sens.* **2022**, *7*, 1235.

[63] G. L. Long, J. D. Winefordner, *Anal. Chem.* **1983**, *55*, 1432.

[64] S. Hurrle, S. Friebe, J. Wohlgemuth, C. Wöll, J. Caro, L. Heinke, *Chemistry* **2017**, *23*, 2294.

[65] J. Buchmann, E. Zhang, C. Scharfenorth, B. Spannekrebs, C. Villringer, J. Laufer, *Evaluation of Fabry-Perot polymer film sensors made using hard dielectric mirror deposition*, **2016**, *9708*, 970856.

[66] P. Beard, T. Mills, *Appl. Opt.* **1996**, *35*, 663.

[67] T. Rajkumar, D. Kukkar, K.-H. Kim, J. R. Sohn, A. Deep, *J. Ind. Eng. Chem.* **2019**, *72*, 50.